

## Charge-neutral, GeV-scale electron-positron pair beams produced using bremsstrahlung gamma rays

Youhwan Noh<sup>1,2,4</sup>, Jaehyun Song<sup>1,2,4</sup>, Mohammad Mirzaie <sup>2,3</sup>, Calin Ioan Hojbota <sup>2</sup>, Hyeong-il Kim<sup>1,2</sup>, Seongmin Lee<sup>1,2</sup>, Junho Won<sup>1,2</sup>, Hoon Song<sup>1,2</sup>, Chiwan Song<sup>1,2</sup>, Chang-Mo Ryu<sup>2</sup>, Chang Hee Nam <sup>1,2</sup> & Woosuk Bang <sup>1,2</sup> 

Matter-antimatter plasmas, such as electron-positron pair plasmas, are frequently observed in various astrophysical phenomena. In laboratory settings, electron-positron pairs have often been generated using high-Z converters irradiated by either direct laser pulses or laser-driven electron beams. Here we generate charge-neutral electron-positron beams with energies in the GeV range, utilizing bremsstrahlung gamma rays. Specifically, intense high-energy gamma rays produced electron-positron pair particles in a lead converter via the Bethe-Heitler process. The produced pair beams exhibited neutrality across all converter thicknesses throughout the energy spectrum spanning from 10 MeV to 1.8 GeV. Pairs with energies surpassing 1 GeV constituted up to 26% of the total kinetic energy within the spectrum. The experimental results were in good agreement with our Geant4 Monte Carlo simulations. These GeV-scale neutral pair particle beams have potential applications for understanding energetic astrophysical phenomena and high-energy particle physics.

<sup>1</sup> Department of Physics and Photon Science, GIST, Gwangju 61005, Korea. <sup>2</sup> Center for Relativistic Laser Science, Institute for Basic Science, Gwangju 61005, Korea. <sup>3</sup> Advanced Photonics Research Institute, GIST, Gwangju 61005, Korea. <sup>4</sup> These authors contributed equally: Youhwan Noh, Jaehyun Song.  
✉ email: [wbang@gist.ac.kr](mailto:wbang@gist.ac.kr)

Electron-positron pair plasmas exhibit distinct characteristics owing to the equal mass of two oppositely charged particles<sup>1–4</sup>. These properties include a reduced charge separation and decreased electrostatic potential fluctuations<sup>1</sup>, which affect the growth and damping of nonlinear plasma instabilities<sup>2,4</sup>. Because these plasmas are composed of two light-pair particles, they are commonly found in the vicinity of energetic astrophysical objects<sup>5</sup>, such as neutron stars<sup>5,6</sup>, quasars<sup>7,8</sup>, black holes<sup>9,10</sup>, and supernova explosions<sup>5,11</sup>. In particular, gamma-ray bursts have been shown to involve electron-positron plasmas as a source<sup>2,12–17</sup>. Thus, creating electron-positron plasmas on a laboratory scale is essential for a clear understanding of various astrophysical phenomena.

In recent studies, several groups have employed high-power lasers to produce positrons and investigate pair plasma dynamics and laboratory astrophysics<sup>2,3,12,18–27</sup>. Two distinct methods have been developed to produce electron-positron pairs using lasers<sup>2,3,12,18–28</sup>. In some experiments, intense laser pulses are focused directly onto a high-Z solid converter to heat electrons above 1 MeV<sup>3,19,20,26</sup>. When the resulting hot electrons collide with the atomic nuclei in the converter, they generate electron-positron pairs through the Trident or Bethe-Heitler processes<sup>20</sup>. In the Trident process, an electron-positron pair is created through the immediate decay of a virtual photon originating from an energetic electron in the nuclear field. On the other hand, the Bethe-Heitler process produces a pair through the conversion of a bremsstrahlung photon emitted from an electron in the nuclear field.

The method described above entails the direct interaction between a laser and a solid target, causing a significant transfer of laser energy to electrons, typically 10–50%<sup>20,29</sup>. Numerous initial hot electrons can generate a substantial number<sup>20,21</sup> of electron-positron pairs on the order of  $10^{10}$ – $10^{12}$ . However, the initial hot electrons exhibit a wide angular spread<sup>22</sup> and a low temperature of several MeV, producing low-density and low-energy-pair particles<sup>20</sup>.

In other experiments, electron-positron pairs are produced in two steps. First, laser pulses are focused on an underdense gas target to accelerate electrons to relativistic energies via the laser wakefield acceleration (LWFA) process<sup>30–34</sup>. Then, these high-energy electron beams enter a high-Z converter to generate electron-positron pairs<sup>2,12,23–25,27,28</sup>. Electron beams accelerated by the LWFA have a small divergence angle of less than several mrad and high energy, ranging from several hundred MeV to 8 GeV<sup>30–33</sup>, and are suitable for producing high-density and high-energy pair particles. However, compared with direct laser-solid interactions, the energy conversion efficiency from the incident laser pulse energy to electron-positron pairs is relatively low<sup>20</sup>, generating fewer pair particles<sup>2</sup> on the order of  $10^7$ .

In both approaches, the resulting beam escaping from the converter consists mainly of electrons because pair production is initiated by numerous energetic electrons that could still pass through the converter. The low ratio of positrons to electrons in the composite beam poses a significant challenge in satisfying charge neutrality, making it difficult to classify the beam as a pair plasma. Several strategies have been implemented in recent experiments to overcome this limitation, such as using a thick converter<sup>2,12</sup> or magnetic collimation<sup>3</sup>. However, adopting a thick converter causes some issues such as high divergence of the pair beam and reduced kinetic energy of the pair particles. The magnetic collimation technique is only efficient within a narrow energy range. For example, the applicable energy range was  $\pm 2$  MeV, centered around 13 MeV in a previous study<sup>3</sup>.

Here we report on the successful generation of charge-neutral GeV electron-positron beams using a multi-PW laser. In our

experiments, strong bremsstrahlung gamma rays from a lead target irradiated by LWFA electrons were selected to enter a lead converter. This method can be a promising approach for obtaining a charge-neutral pair particle beam, regardless of the converter thickness or pair particle energy. When photons with energies greater than 10 MeV pass through a high-Z material, pair production starts to predominate over other interaction processes between photons and atoms. In Bethe-Heitler processes, electron-positron pairs are created with a nearly symmetrical energy distribution<sup>35</sup>, and the stopping powers of the two particles are almost identical<sup>36</sup>, resulting in similar changes in their energy spectra over a wide range of converter thicknesses.

## Results and Discussion

**LWFA electron beams.** Figure 1 shows the LWFA electron energy spectra obtained using a 1.3 T magnet. A raw data image of the Lanex3 screen used for electron energy measurements is shown in Fig. 1a. Figure 1b depicts six different energy spectra (pink lines) of the incident LWFA electrons and their average spectrum (black line) obtained using both Lanex2 and Lanex3. The energy spectra of the input electron beam on Lanex screens were measured without the bremsstrahlung target prior to the pair production experiments since the bremsstrahlung target distorts the energy spectra of the input electron beam. We used Lanex2 data to measure the electron energy spectra from 320 to 750 MeV and Lanex3 data to obtain the energy spectra above 750 MeV. Most electron beams exhibited a local energy peak at approximately 2 GeV and an average divergence angle of 1.4 mrad. The total charge of the input electron beam above 320 MeV was  $950 \pm 320$  pC on average, and the high energy electrons above 1 GeV accounted for  $175 \pm 99$  pC in Fig. 1b. This corresponds to an average incident electron beam energy of more than 700 mJ, with GeV electrons carrying approximately 250 mJ of the total energy (see Supplementary Table 1 for details).

**Imaging plate from the experiment.** Figure 2 shows five-shot accumulated photostimulated luminescence (PSL) images for the 3 mm converter. The dashed white lines in the image mark the region where the divergence half-angle from the center of the converter is within the collimator's acceptance angle of 8 mrad. Figure 2a, b show PSL images on the imaging plate (IP) installed on the electron and positron sides of the magnet, respectively. Figure 2c, d depict oppositely charged particles on either side of the near IP and far IP. The PSL images recorded in Fig. 2c, d agree very well with the predicted magnetic deflections of electrons and positrons within the spectrometer. By having two IPs on the front surfaces, we verified that the PSL images in Fig. 2c, d indeed originated from electrons and positrons not from noise or background artifacts.

The PSL values within the region delineated by the dashed white line for each column were summed to reconstruct the energy spectra of the electron-positron pairs. The sum of PSL in each column, divided by the PSL response, yields the number of particles. The corresponding energy can be calculated from the position of the column. The PSL response to electron and gamma radiation has been determined in previous studies<sup>37,38</sup>. The calibrated PSL response of electrons can be used for positrons as well because the deposited energies from electrons and positrons in the IP are nearly the same (within 2%)<sup>12,24,36</sup>.

**Imaging plate from the Geant4 simulation.** Geant4 simulations were performed to compare with the experimental results<sup>39</sup>. The energy spectrum and divergence angle obtained by the Lanex screens were used as the initial electron beam parameters in the

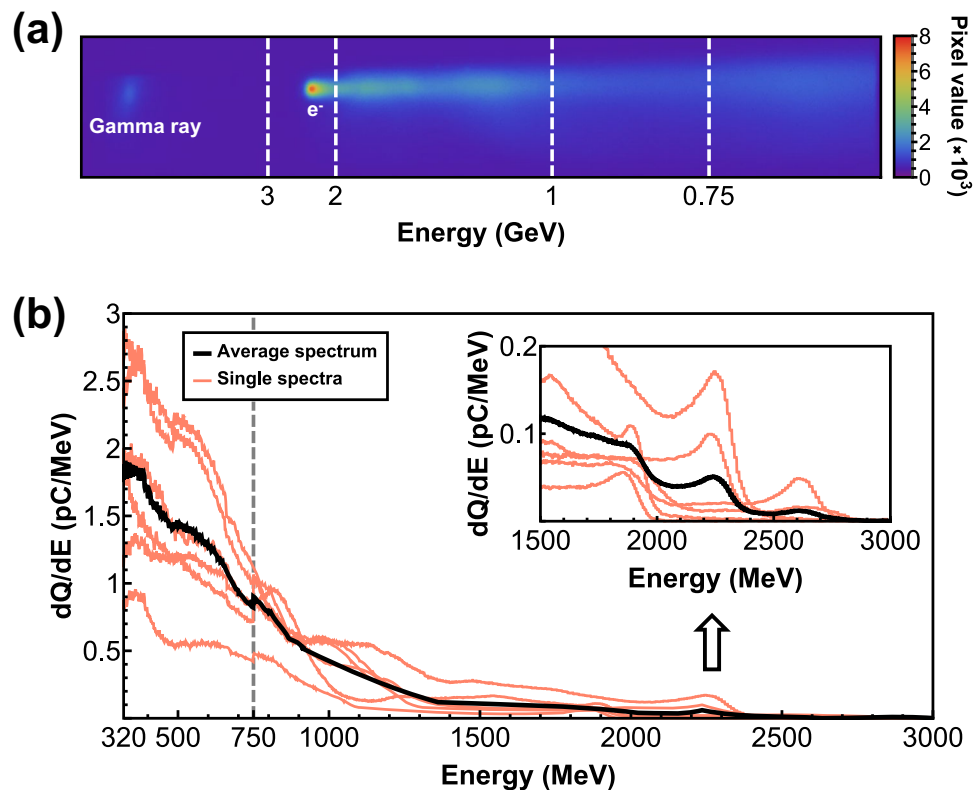


**Fig. 1 Measured energy spectra of initial electron beams.** **a** Raw image of Lanex3 screen showing the electron energy spectrum obtained without the bremsstrahlung target. A dim spot on the left-hand side indicates the gamma rays emitted from the electrons passing through the aluminum foil installed to block the transmitted laser beam after the LWFA. **b** Measured electron energy spectra for six shots are shown along with their average spectrum. The pink lines show single-shot energy spectra. The black line shows the average electron energy spectrum. The energy spectra for energy regions above and below 750 MeV were calculated using the data of Lanex3 and Lanex2, respectively. The inset shows the spectra above 1.5 GeV.

simulations, and the number of initial electrons was set to 10 million, with the direction of the beam fixed at the center of the bremsstrahlung converter. Geant4 simulations were performed for each lead-converter (in air) thickness, including lead collimators and spectrometer structures in air.

Figure 3 illustrates the calculated PSL images obtained from our Geant4 simulations using a 3-mm-thick lead converter. Geant4 simulations recorded the energy, position, and momentum vectors of three types of radiation (electrons, positrons, and gamma rays) passing through the planes in which the IPs were installed. The PSL values recorded in each 1 mm × 1 mm pixel were calculated using the known PSL response, which varied according to the radiation energy and incidence angle<sup>37,38,40</sup>. Figures 3a, d, and g show the PSL images generated from all radiations along with the contributions of electrons and positrons originating from the lead converter. We calculated the projected trajectories of the pair particles based on the recorded position and momentum vectors at the collimator exit to isolate pair particles originating from the converter.

In Figs. 3b, c, e, f, h, and i, we obtained the noise PSL for each column and row by subtracting the PSL generated by pair particles produced within the converter from the total PSL. The background noise of electrons closely matched that of positrons at the front IPs within 7%. At the side IP, the background noise of electrons was found to be larger than that of positrons by about 15%. The noise distribution exhibits position dependence along the x-axis, which is the direction in which the magnetic field bends the particle trajectory. However, this position dependence was relatively weak on the y-axis. The noise of the experimental data was subtracted according to the trends we found in the simulations (see Supplementary Fig. 1 for details).

**Analysis of produced electrons and positrons.** The energy range was divided into three parts, and each energy spectrum was calculated from different IPs. Energy spectra ranging from 10 to 280 MeV were obtained using the side IPs. The near IP was used for particles with energies above 280 MeV and below 1 GeV. When using the near IP for particles with energies greater than 1 GeV, it was difficult to distinguish the pair particle signals from the central gamma rays. To obtain the energy spectra of the high-energy part, we used a far IP installed 40 cm after the near IP. This additional IP enhanced the spectral resolution for kinetic energies above 1 GeV.

Figure 4a, b show the measured energy spectra of electrons and positrons, respectively. The top image in Fig. 4a shows the combined image of all three IP measurements for the electrons. The PSL images from the side IP, near IP, and far IP were stitched together to create a single combined PSL image, from which the measured energy spectrum of electrons was obtained, as shown on the bottom plot. The predicted energy spectrum from Geant4 simulations is also shown on the same plot for comparison. The number of measured electrons and positrons in the energy range from 10 MeV to 1.8 GeV is  $1.9_{-0.7}^{+0.6} \times 10^6$  and  $2.0_{-0.8}^{+0.7} \times 10^6$ , respectively, which confirms the generation of charge-neutral pair particles in our experiment (see Supplementary Figs. 2–4 for similar analysis using other converter thicknesses).

In Fig. 4a, b, the measured energy spectra of both electrons and positrons peak at approximately 100 MeV. Around 6% of the total electrons and positrons have kinetic energies larger than 1 GeV. Remarkably, we find that these particles with kinetic energies above 1 GeV account for about 20% (= 49  $\mu$ J) of the

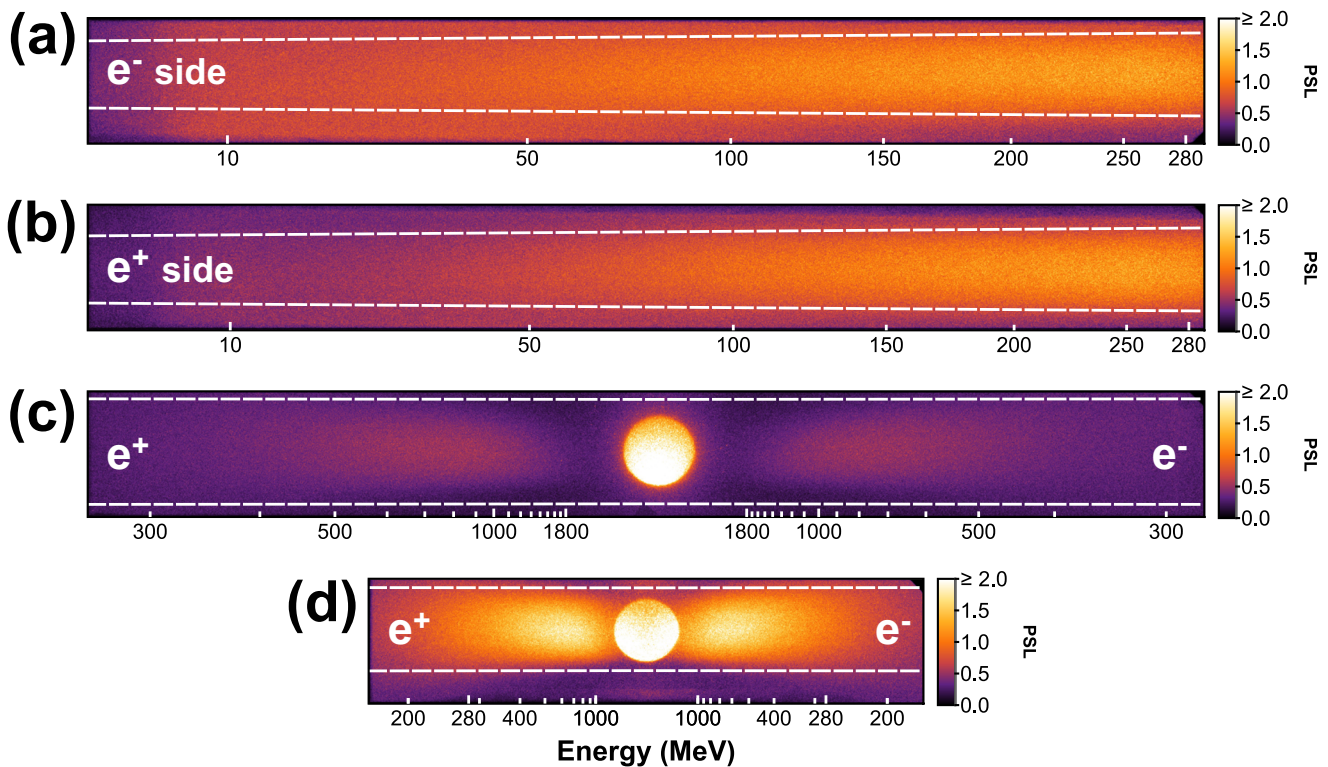


**Fig. 2 Five-shot-accumulated PSL images for a 3 mm lead converter.** **a** Electrons were detected on the side IP. **b** Positrons were detected on the other side IP. **c** The far IP recorded electrons, positrons, and gamma rays. Above-GeV electrons and positrons are clearly visible on the far IP. **d** The near IP detected electrons, positrons, and gamma rays with a lower energy resolution. The effective data region permitted by the collimators is indicated by horizontal white dashed lines in the figures.

total kinetic energy ( $= 251 \mu\text{J}$ ) of the pair particles. When using a 6-mm lead converter, 9% of the total particles are above-GeV electrons and positrons, carrying 26% of the total kinetic energy (see Supplementary Fig. 5 for details). This is a relatively large fraction compared with the incident electron beam with energy higher than 1 GeV, as shown in Fig. 1. This is explained by the energy dependence of the divergence angle of the pair particles: The divergence angle is known to be inversely proportional to the Lorentz factor of the particle<sup>22,24</sup>. Consequently, high-energy pair particles have small divergence angles, and many of them are detected at the IPs. This behavior was also observed in the Geant4 simulations.

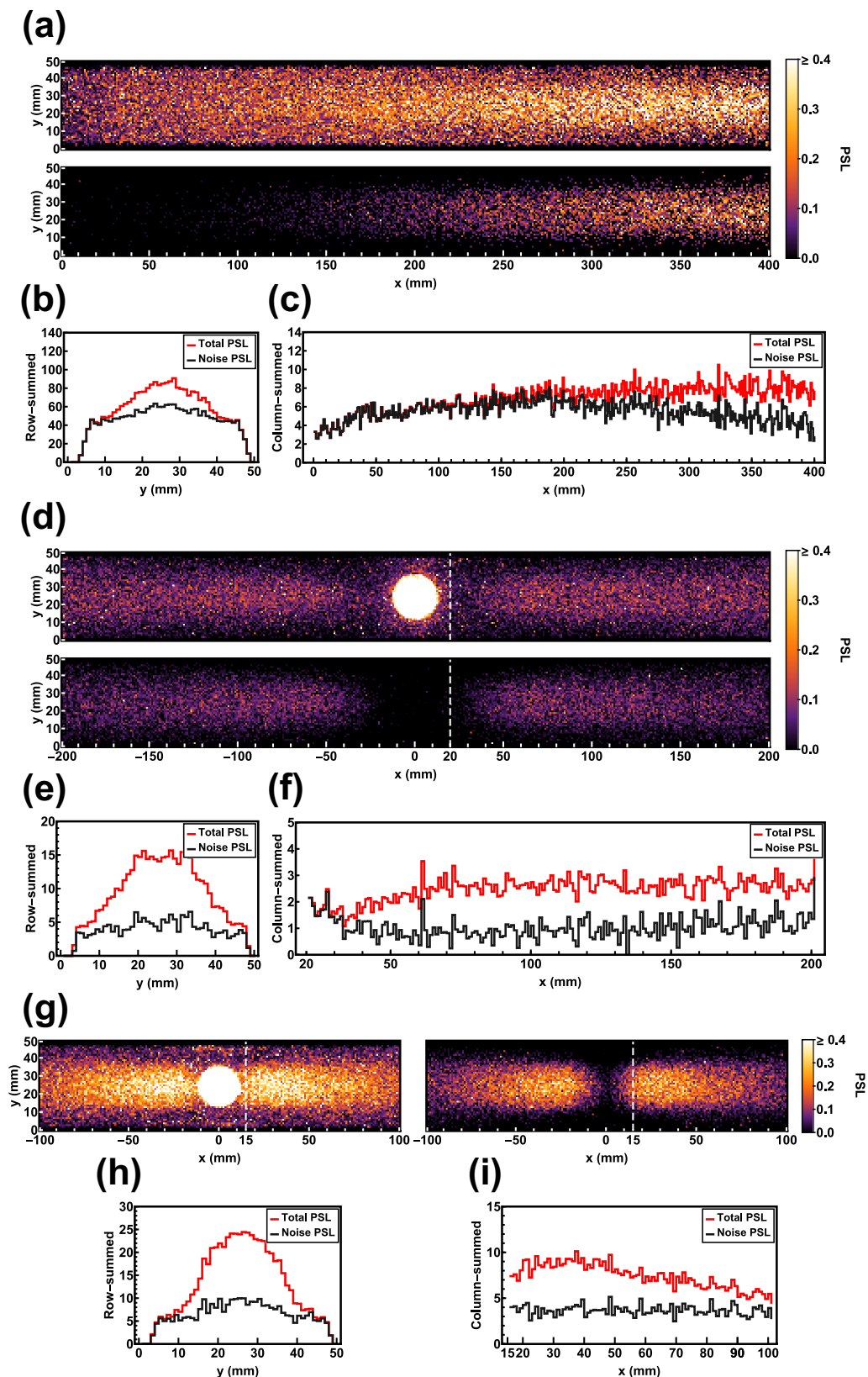
The measured energy spectra from the experiment were compared with those obtained from the PSL images in the Geant4 simulations in Fig. 4a, b. Both energy spectra peaked at around 100 MeV, and the number of generated pair particles decreased gradually with increasing energy. Since the number of initial electrons in the simulations was fixed at 10 million, we multiplied the energy spectra obtained from the simulations by a scaling factor in order to match the total number of pair particles obtained from both experiments and simulations.

Figure 5 shows the average energy spectra of electrons and positrons obtained over five consecutive shots for different lead converter thicknesses: (a) 3 mm, (b) 6 mm, (c) 9 mm, and (d) 15 mm. The experiments were conducted under similar conditions for each converter thickness. To account for the fluctuations in the LWFA electron beam quality, we normalized the generated pair particle numbers based on the relative amount of input gamma rays measured from the LYSO detector with respect to the 3 mm converter case.

Note that the energy spectrum shifts towards the lower energy region for thicker converters. This can be understood as a result

of the increased probabilities of energy loss and cascade processes when the generated pair particles traverse the remaining part of the converter<sup>2</sup>. Intriguingly, the energy spectra of electrons and positrons are found to be nearly identical for all converter thicknesses, which suggest charge neutrality at every energy interval. The charge neutrality, which represents the number ratio of positrons in the electron-positron beam, is also plotted in Fig. 5. The charge neutralities for energies exceeding 1 GeV exhibit relatively larger fluctuations, which can be attributed to the limited number of high-energy particles detected by the far IPs. This results in larger errors during the noise subtraction process for each column. Despite this limitation, the pair particle beams produced in the converter exhibit charge neutrality across all converter thicknesses for every energy interval in the entire energy spectrum from 10 MeV to 1.8 GeV.

By integrating the energy spectra shown in Fig. 5a–d, we computed the electron and positron yields at each converter thickness. Figure 6a, b show the electron and positron yields as functions of the converter thicknesses obtained from the Geant4 simulations (red triangles) and experiments (hollow black circles). In Fig. 6a, b, the red triangles represent the simulation results multiplied by a common scaling factor to match the total number of pair particles measured from experiments using four different lead converters. There are some deviations between the measured and simulated pair particle yields in Fig. 6a, b. We speculate that this is caused by the fluctuations in the incident LWFA electron beams, as illustrated in Fig. 1. Our measurements are consistent with the simulation results, within experimental uncertainties. Figure 6c represents the charge neutrality for different converter thicknesses, which demonstrates that the pair particles generated using energetic gamma rays are charge neutral regardless of the converter thickness.



**Fig. 3** Calculated PSL images using Geant4 simulations for a 3-mm-thick lead converter. **a** Calculated PSL image of the electron-side IP (top). Noise-subtracted PSL image (bottom). **b** Row-summed PSL of the electron-side IP. **c** Column-summed PSL of the electron-side IP. **d** Calculated PSL image of far IP (top). Noise-subtracted PSL image (bottom). **e** Row-summed PSL of the far IP. **f** Column-summed PSL of the far IP. **g** Calculated PSL image of near IP (left). Noise-subtracted PSL image (right). **h** Row-summed PSL of the near IP. **i** Column-summed PSL of the near IP. The two images of each subplot of **(a)**, **(d)**, and **(g)** show the PSL image generated by all radiations and generated only by pair particles produced within the lead converter, respectively. The summation of the near and far IP was performed only in the region corresponding to the electrons, the right side of the white dashed lines on the PSL image.

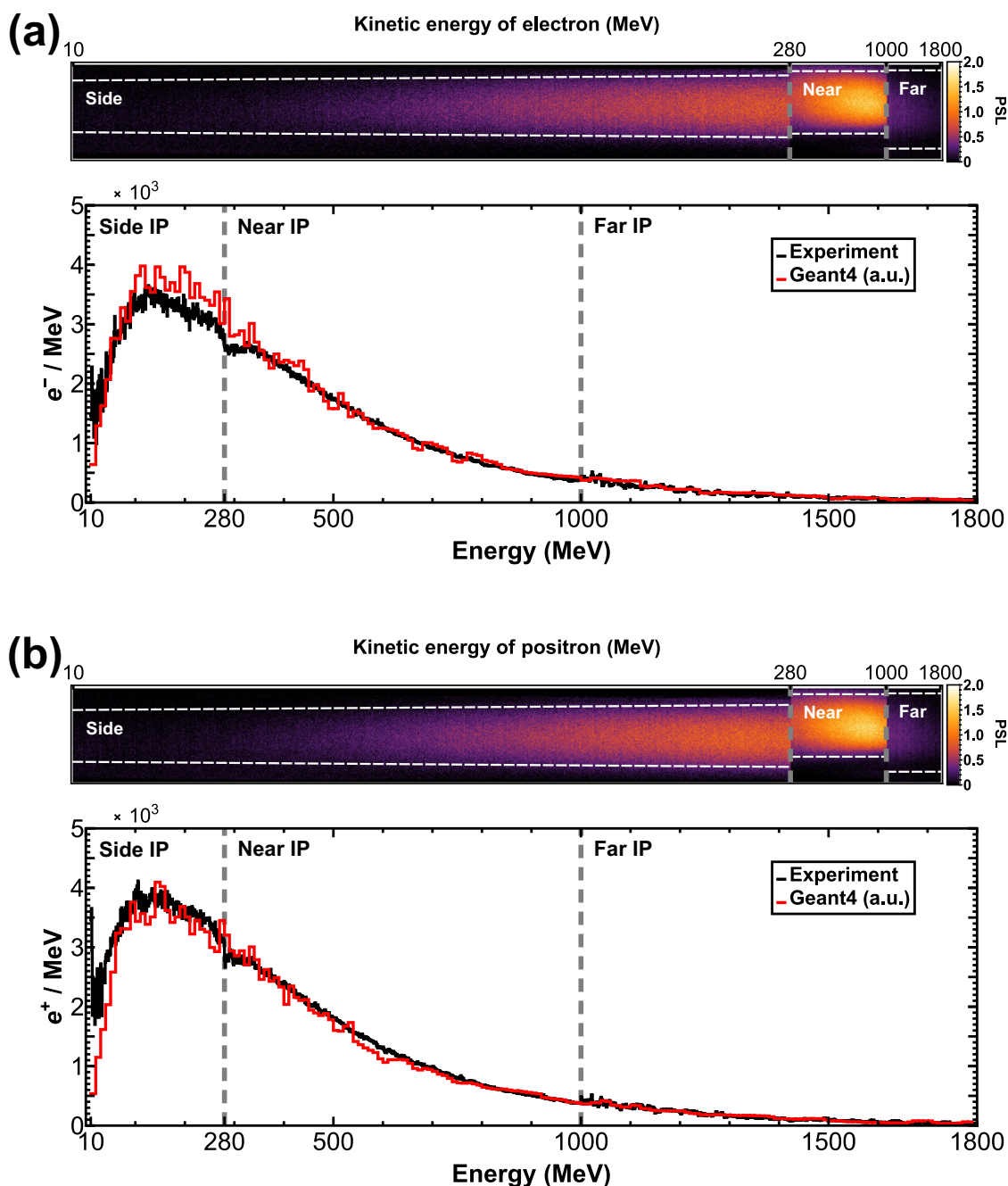


**Fig. 4 Comparison between experiments and Geant4 simulations for the 3 mm lead converter.** Noise-subtracted experimental IP PSL images for the 3 mm lead converter and reconstructed energy spectra for (a) electrons and (b) positrons. The horizontal dashed white lines in the IP PSL images represent the effective data regions permitted by the collimators. The energy spectra obtained from noise-subtracted IPs in the experiments (black lines) for the average of five consecutive shots are plotted with the energy spectra obtained from noise-subtracted PSL images in the Geant4 simulations (red lines), which were scaled to match the experimental results. The energy resolution of the simulation is 10 MeV. The energy spectra were calculated using the side IP (10–280 MeV), near IP (280 MeV to 1.0 GeV), and far IP (1.0–1.8 GeV).

We performed additional analysis of Geant4 simulations to estimate the number density of the pair particle beams. We calculated the spatial distributions of pair particles, and estimated the particle density at 1 cm after the converter and at the exit of the second collimator. Since pair particles passing through the 2 cm diameter collimator hole were detected in our experiments, we defined a cylindrical volume of a 2 cm diameter at these two locations. The longitudinal length of the cylinder was set to 50  $\mu\text{m}$ , which contained  $\sim 50\%$  of the particles passing through the hole at the collimator exit.

In our experiments, we have produced  $3.9^{+1.3}_{-1.5} \times 10^6$  pair particles per shot using a 3-mm thick lead converter. For this converter thickness, Geant4 predicted that 57% of the detected pair particles would be within the cylindrical volume at the second collimator exit, resulting in a number density of  $1.4 \times 10^8 \text{ cm}^{-3}$ . Geant4 calculations estimated that the number density near the converter ( $= 1.4 \times 10^9 \text{ cm}^{-3}$ ) was approximately ten times higher than that at the collimator exit.

In a previous study that used energetic electrons as the seed beam for pair production, the optimum converter thickness

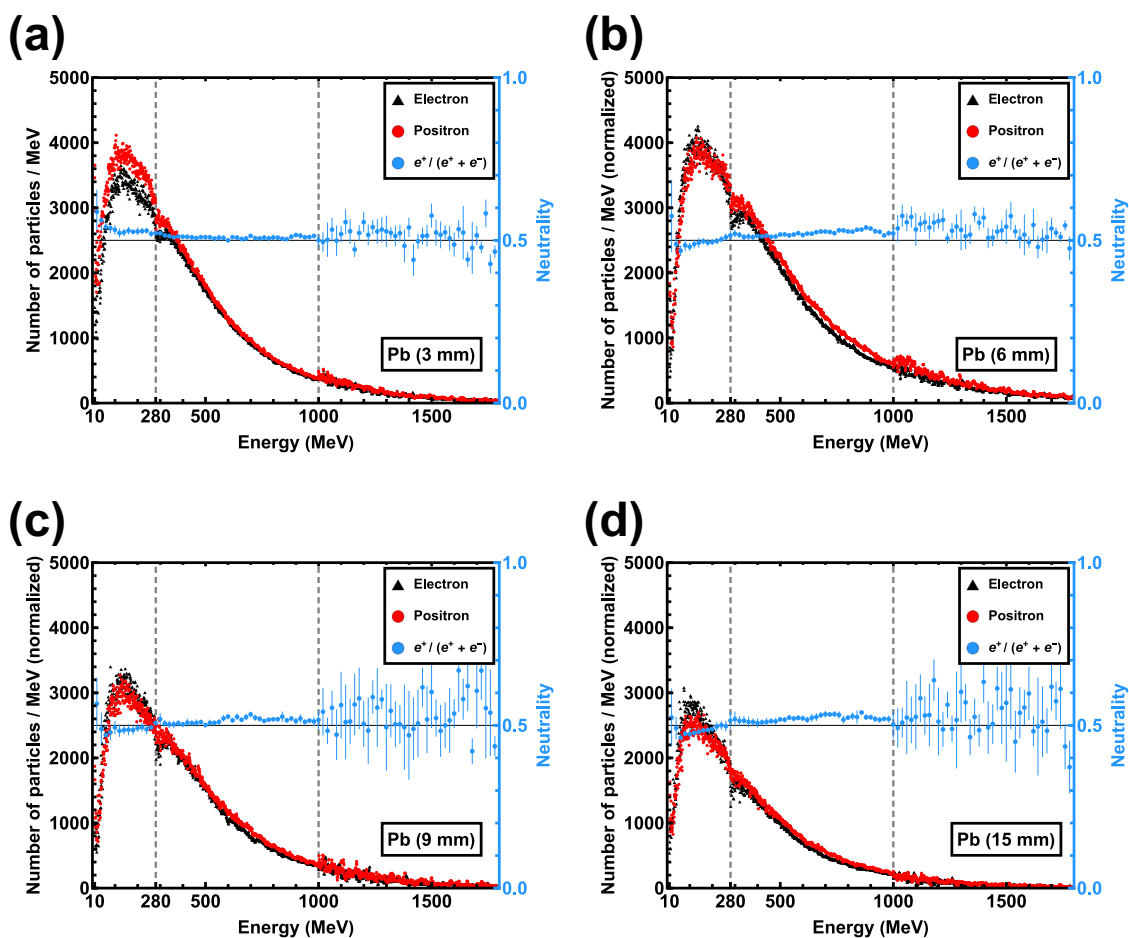


**Fig. 5 Energy spectra and charge neutralities of pair particle beams.** Measured electron (black triangles) and positron (red circles) energy spectra, averaged over five consecutive shots, for the converter thickness of (a) 3 mm, (b) 6 mm, (c) 9 mm, and (d) 15 mm. Energy spectra of pair particles in (b–d) were normalized to the relative amount of input gamma rays on the converter with respect to the 3 mm converter case. The blue circles show charge neutrality in a 20 MeV energy interval for each plot. The error bars indicate the standard deviation of twenty charge neutralities with 1 MeV resolution (see Supplementary Fig. 6 for charge neutralities with 1 MeV resolution).

varied depending on the desired conditions of the pair beam<sup>2</sup>. A relatively thick converter was required to achieve charge neutrality close to 0.5. However, the energy loss and divergence increased for the thick converter, resulting in a reduced kinetic energy and large divergence of the generated pair particle beam. The optimum converter thicknesses for maximum energy, maximum yield, and charge neutrality of 0.5 were found to be 1, 2, and 5 radiation lengths, respectively<sup>2</sup>. In comparison, our experiments confirmed that if high-energy gamma rays are employed as seeds, GeV-scale charge-neutral pair beams could be achieved even with a thin converter.

## Conclusions

We successfully generated charge-neutral electron-positron pair beams using high-energy bremsstrahlung gamma rays with a multi-PW laser and a lead converter of different thicknesses (3, 6, 9, and 15 mm). Our experimental results showed that the number of pair particles tend to decrease as the lead converter became thicker, with a maximum value at 6 mm. Their energy spectra showed a peak energy of approximately 100 MeV, and particles with kinetic energies above 1 GeV carried up to 26% of the total kinetic energy for a 6 mm converter.

We generated pair-particle beams consisting of almost equal numbers of electrons and positrons with energies above 1 GeV using energetic gamma rays. These charge-neutral GeV electron-

positron beams could be achieved even with a thin converter. This is a unique feature compared with the conventional method that uses a single target for both bremsstrahlung and pair production. While the resulting particle density was relatively low ( $1.4 \times 10^9 \text{ cm}^{-3}$ ) because of the additional conversion and filtering steps required to select pure gamma rays, this method represents an important step forward in the generation of high-energy neutral pair plasmas required for investigating astrophysical phenomena at the laboratory scale.

## Methods

**Pair production from gamma rays.** We conducted pair production experiments using a multi-PW laser<sup>41</sup> at the Center for Relativistic Laser Science (CoReLS). The experimental setup consisted of two sections. The first section included an LWFA setup that generates a multi-GeV electron beam, which was directed into a 4-mm-thick lead target to produce strong bremsstrahlung gamma rays. The second section was designed to generate electron-positron pairs by irradiating a lead converter with the high-energy gamma rays generated in the first section.

An experimental schematic of the gamma-ray generation is shown in Fig. 7a. An  $f/43$  spherical mirror with a focal length of 12 m focused the laser beam into a 5-cm-long gas cell containing helium gas doped with 3% neon at a backing pressure of 1.5 bar, corresponding to an electron density of  $7 \times 10^{17} \text{ cm}^{-3}$ . The focal

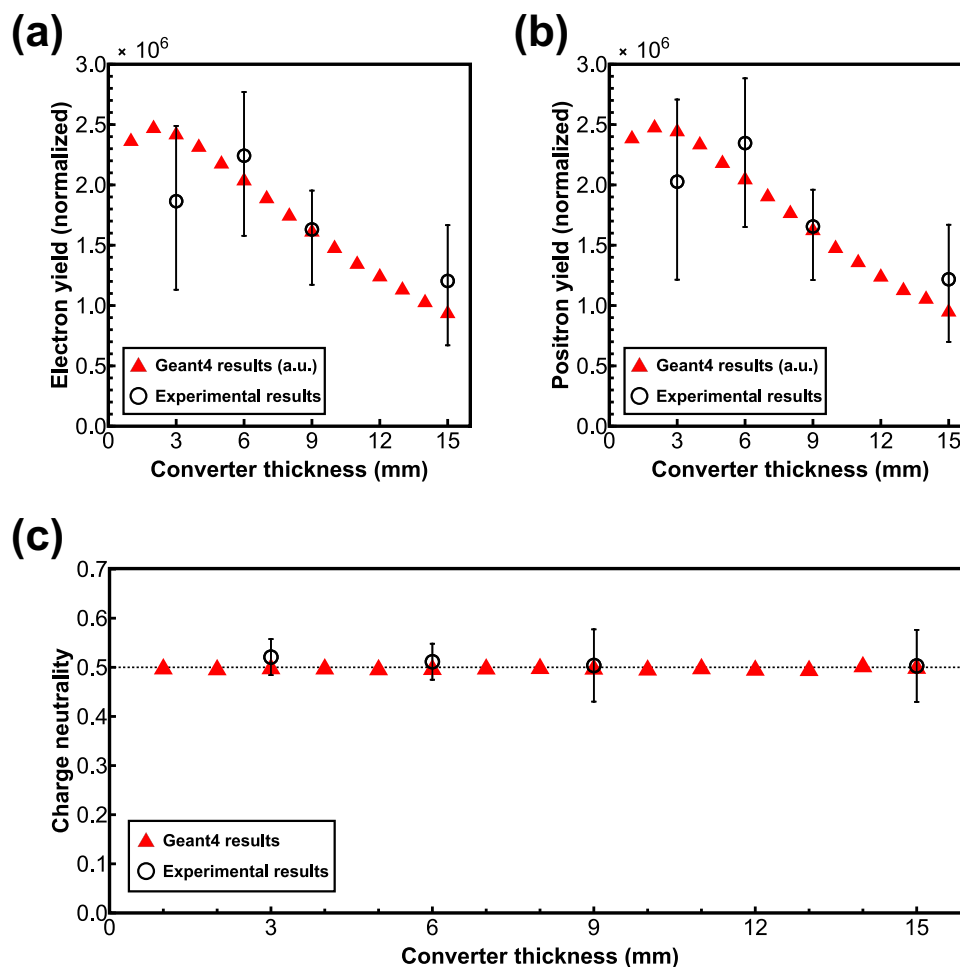


**Fig. 6 Pair particle yields vs. converter thicknesses.** **a** Measured electron and **(b)** positron yields (hollow black circles) are plotted for different converter thicknesses. The total particle yields were normalized to the relative amount of input gamma rays on the converter with respect to the 3 mm converter case. The error bars were calculated from the variation of noise PSL in the vertical axis, discontinuities in the energy spectrum at around 280 MeV, and the standard deviations of the total pixel value of the LYSO image in the corresponding area of the converter on the LYSO. Geant4 simulation results (solid red triangles) were scaled to match the total particle number of the experimental results at four different thicknesses of lead converters. **c** Measured charge neutrality is shown as a function of the converter thickness varying from 3 to 15 mm. The error bars indicate the standard deviation of charge neutrality in 1 MeV resolution. Geant4 simulation results (solid red triangles) are also shown for 1 to 15 mm converter thicknesses.

spot size was  $47 \mu\text{m}$  (FWHM), which contained an energy of 14.6 J with a pulse duration of 25 fs, where the corresponding laser intensity was  $\sim 3.0 \times 10^{19} \text{ W cm}^{-2}$ . The electrons in the gas cell were accelerated up to energies of several GeV by relying on the LWFA in the nonlinear regime, while the gas mixture was chosen to facilitate electron injection into the wakefield through an ionization injection scheme<sup>42–44</sup>.

Three phosphor screens (Lanex) imaged onto the CCDs were used to characterize the properties of the relativistic electron beams. Lanex1 was placed at the magnet entrance to measure the pointing angle and divergence of the accelerated electrons. Lanex2 and Lanex3 were installed after a 1.3 T magnet to obtain the energy spectra of the accelerated electrons considering the pointing angle obtained from the Lanex1 screen.

The 4-mm-thick lead target was positioned behind Lanex1 to produce intense high-energy bremsstrahlung photons. The initial electron beams that passed through the lead target and the charged particles that were generated within the lead target were deflected by a 1.3 T magnet (see Supplementary Fig. 7 for particles generated within the lead target). Consequently, only gamma rays exited the vacuum chamber through a Mylar window with a thickness of 200  $\mu\text{m}$ . Outside the window, a 5-mm-thick

Lutetium-yttrium oxyorthosilicate (LYSO), or a gamma-ray scintillation crystal<sup>45</sup>, was installed to measure the pointing of the transmitted gamma rays.

Figure 7b illustrates the experimental schematic of electron-positron pair production from strong gamma rays. The converter for producing electrons and positrons was placed 1.4 m from the Mylar window in the air. Lead plates of different thicknesses were used as converters ( $d = 3, 6, 9,$  and  $15 \text{ mm}$ ). Within the lead converter, high-energy photons interact with atomic nuclei to produce electron-positron pairs via the Bethe-Heitler process.

**Pair spectrometer.** The two collimators accepted particles with a divergence half-angle of less than 8 mrad from the center of the back surface of the converter (see Supplementary Fig. 8 for details). The first collimator was fabricated by drilling a hole with a diameter of 2 cm through a block of pure lead. The second collimator also had a 2 cm diameter hole, which was constructed using a lead cylinder with a 4 cm diameter hole coated with a 1-cm-thick layer of stainless steel. A two-collimator setup was shown to be desirable for the measurement of electron-positron pairs generated in the GeV regime, minimizing the noise on the detectors<sup>46</sup>.

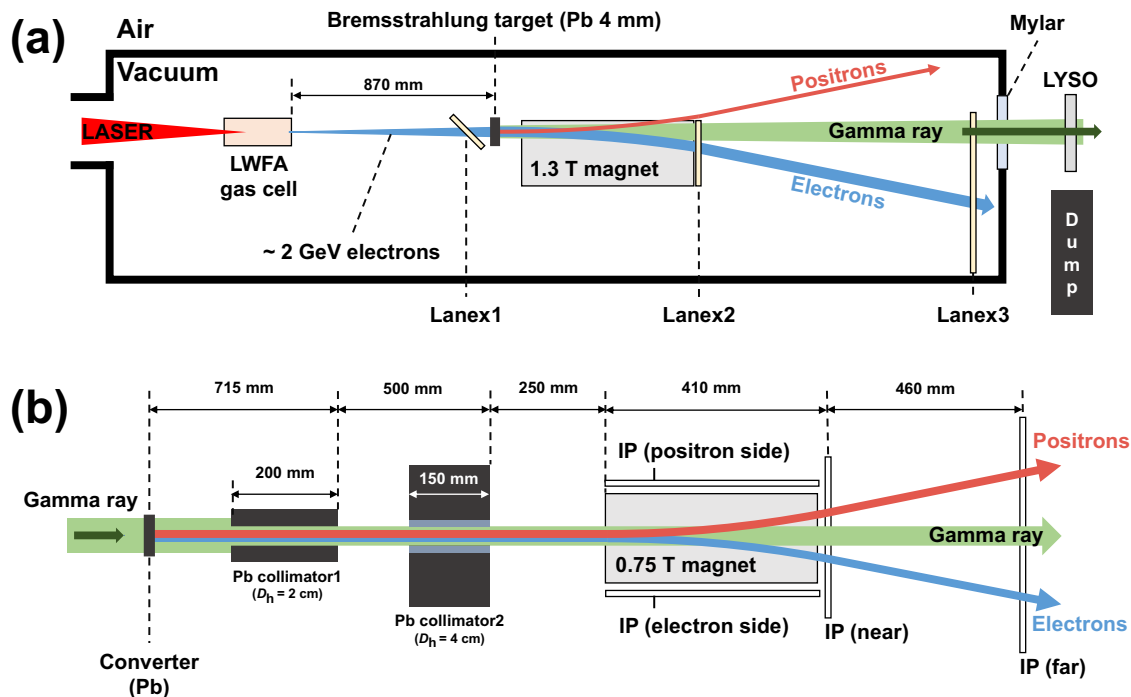


**Fig. 7 Experimental setup.** **a** LWFA scheme: Gamma rays are produced via bremsstrahlung radiation of relativistic electron beams in a 4-mm-thick lead target. A 1.3 T dipole magnet deflects all the charged particles (LWFA electrons and pair particles), and only gamma rays are allowed to propagate further towards the lead converter installed in the air. Lutetium-yttrium oxyorthosilicate (LYSO) was installed to measure the pointing of the transmitted gamma rays. **b** Pair production scheme: Electrons and positrons are produced via the Bethe-Heitler process in the lead converter. The energy spectra of pairs are measured by two IPs installed at the sides of the 0.75 T dipole magnet and two more IPs (near & far IPs) after the magnet.

The pair spectrometer consisted of a 0.75 T permanent dipole magnet with a 4 cm gap and a set of four IPs. IPs can detect electrons and positrons, and particle fluence can be calculated from PSL images. Two 40-cm-long side IPs were installed on both sides of the magnet, and electrons and positrons with kinetic energies ranging from 10 to 280 MeV were detected. A 20-cm-long IP (near IP) was placed at the exit of the magnet to measure electrons and positrons with kinetic energies above 280 MeV. Furthermore, another 40-cm-long IP (far IP) after the near IP measured particles with kinetic energies above 1 GeV. We used Fuji BAS-MS IPs, and each IP was wrapped with a 50- $\mu$ m-thick black aluminum foil to prevent the loss of PSL induced by ambient lights. The entire set of IPs was scanned together for 10–15 min after accumulating five consecutive laser shots at each lead converter thickness. The PSL results were calculated with fading effects taken into account<sup>47,48</sup>.

### Data availability

The data that support the findings of this study are available from the corresponding author upon reasonable request.

Received: 1 September 2023; Accepted: 4 January 2024;

Published online: 29 January 2024

### References

- Stoneking, M. R. et al. A new frontier in laboratory physics: Magnetized electron–positron plasmas. *J. Plasma Phys.* **86**, 155860601 (2020).
- Sarri, G. et al. Generation of neutral and high-density electron–positron pair plasmas in the laboratory. *Nat. Commun.* **6**, 6747 (2015).
- Peebles, J. L. et al. Magnetically collimated relativistic charge-neutral electron–positron beams from high-power lasers. *Phys. Plasmas* **28**, 074501 (2021).
- Surko, C. M. & Greaves, R. G. Emerging science and technology of antimatter plasmas and trap-based beams. *Phys. Plasmas* **11**, 2333–2348 (2004).
- Thoma, M. H. Ultrarelativistic electron–positron plasma. *Eur. Phys. J. D.* **55**, 271–278 (2009).
- Cerutti, B. & Beloborodov, A. M. Electrodynamics of pulsar magnetospheres. *Space Sci. Rev.* **207**, 111–136 (2017).
- Wardle, J. F. C., Homan, D. C., Ojha, R. & Roberts, D. H. Electron–positron jets associated with the quasar 3c279. *Nature* **395**, 457–461 (1998).
- Sikora, M. & Madejski, G. On pair content and variability of subparsec jets in quasars. *Astrophys. J.* **534**, 109 (2000).
- Mościbrodzka, M., Gammie, C. F., Dolence, J. C. & Shiohawa, H. Pair production in low-luminosity galactic nuclei. *Astrophys. J.* **735**, 9 (2011).
- Takahara, F. & Kusunose, M. Electron–positron pair production in a hot accretion plasma around a massive black hole. *Prog. Theor. Phys.* **73**, 1390–1400 (1985).
- Hardy, S. J. & Thoma, M. H. Neutrino–electron processes in a strongly magnetized thermal plasma. *Phys. Rev. D.* **63**, 025014 (2000).
- Xu, T. et al. Ultrashort mega-electronvolt positron beam generation based on laser-accelerated electrons. *Phys. Plasmas* **23**, 033109 (2016).
- Piran, T. The physics of gamma-ray bursts. *Rev. Mod. Phys.* **76**, 1143–1210 (2005).
- Mészáros, P. Gamma-ray bursts. *Rep. Prog. Phys.* **69**, 2259 (2006).
- Chang, P., Spitkovsky, A. & Arons, J. Long-term evolution of magnetic turbulence in relativistic collisionless shocks: Electron–positron plasmas. *Astrophys. J.* **674**, 378 (2008).
- Gruzinov, A. Gamma-ray burst phenomenology, shock dynamo, and the first magnetic fields. *Astrophys. J.* **563**, L15 (2001).
- Ruffini, R., Vereshchagin, G. & Xue, S.-S. Electron–positron pairs in physics and astrophysics: From heavy nuclei to black holes. *Phys. Rep.* **487**, 1–140 (2010).
- Warwick, J. et al. Experimental observation of a current-driven instability in a neutral electron–positron beam. *Phys. Rev. Lett.* **119**, 185002 (2017).
- Chen, H. et al. Magnetic collimation of relativistic positrons and electrons from high intensity laser–matter interactions. *Phys. Plasmas* **21**, 040703 (2014).

20. Liang, E. et al. High  $e^+ / e^-$  ratio dense pair creation with  $10^{21} \text{w} \cdot \text{cm}^{-2}$  laser irradiating solid targets. *Sci. Rep.* **5**, 13968 (2015).
21. Chen, H. et al. Scaling the yield of laser-driven electron-positron jets to laboratory astrophysical applications. *Phys. Rev. Lett.* **114**, 215001 (2015).
22. Sarri, G. et al. Laser-driven generation of collimated ultra-relativistic positron beams. *Plasma Phys. Controlled Fusion* **55**, 124017 (2013).
23. Gahn, C. et al. Generation of mev electrons and positrons with femtosecond pulses from a table-top laser system. *Phys. Plasmas* **9**, 987–999 (2002).
24. Williams, G. J., Pollock, B. B., Albert, F., Park, J. & Chen, H. Positron generation using laser-wakefield electron sources. *Phys. Plasmas* **22**, 093115 (2015).
25. Sarri, G. et al. Table-top laser-based source of femtosecond, collimated, ultrarelativistic positron beams. *Phys. Rev. Lett.* **110**, 255002 (2013).
26. Cowan, T. E. et al. High energy electrons, nuclear phenomena and heating in petawatt laser-solid experiments. *Laser Part. Beams* **17**, 773–783 (1999).
27. Kim, H. et al. Electron-positron generation by irradiating various metallic materials with laser-accelerated electrons. *Results in Physics* **57**, 107310 (2024).
28. Song, H. et al. Characterization of relativistic electron-positron beams produced with laser-accelerated gev electrons. *Sci. Rep.* **13**, 310 (2023).
29. Levy, M. C., Wilks, S. C., Tabak, M., Libby, S. B. & Baring, M. G. Petawatt laser absorption bounded. *Nat. Commun.* **5**, 4149 (2014).
30. Leemans, W. P. et al. Gev electron beams from a centimetre-scale accelerator. *Nat. Phys.* **2**, 696–699 (2006).
31. Kim, H. T. et al. Enhancement of electron energy to the multi-gev regime by a dual-stage laser-wakefield accelerator pumped by petawatt laser pulses. *Phys. Rev. Lett.* **111**, 165002 (2013).
32. Leemans, W. P. et al. Multi-gev electron beams from capillary-discharge-guided subpetawatt laser pulses in the self-trapping regime. *Phys. Rev. Lett.* **113**, 245002 (2014).
33. Gonsalves, A. et al. Petawatt laser guiding and electron beam acceleration to 8 gev in a laser-heated capillary discharge waveguide. *Phys. Rev. Lett.* **122**, 084801 (2019).
34. Tajima, T. & Dawson, J. M. Laser electron accelerator. *Phys. Rev. Lett.* **43**, 267–270 (1979).
35. Bethe, H., Heitler, W. & Dirac, P. A. M. On the stopping of fast particles and on the creation of positive electrons. *Proc. R. Soc. Lond. Ser. A, Contain. Pap. A Math. Phys. Character* **146**, 83–112 (1934).
36. Rohrlich, F. & Carlson, B. C. Positron-electron differences in energy loss and multiple scattering. *Phys. Rev.* **93**, 38–44 (1954).
37. Boutoux, G. et al. Validation of modelled imaging plates sensitivity to 1–100 kev x-rays and spatial resolution characterisation for diagnostics for the “petawatt aquitaine laser”. *Rev. Sci. Instrum.* **87**, 043108 (2016).
38. Boutoux, G. et al. Study of imaging plate detector sensitivity to 5–18 mev electrons. *Rev. Sci. Instrum.* **86**, 113304 (2015).
39. Agostinelli, S. et al. Geant4—a simulation toolkit. *Nucl. Instrum. Methods Phys. Res. Sect. A: Acceler. Spectro. Detect. Assoc. Equip.* **506**, 250–303 (2003).
40. Rabhi, N. et al. Calibration of imaging plates to electrons between 40 and 180 mev. *Rev. Sci. Instrum.* **87**, 053306 (2016).
41. Sung, J. H. et al. 4.2 pw, 20 fs ti:Sapphire laser at 0.1 hz. *Opt. Lett.* **42**, 2058–2061 (2017).
42. Mirzaie, M. et al. Demonstration of self-truncated ionization injection for gev electron beams. *Sci. Rep.* **5**, 14659 (2015).
43. Pak, A. et al. Injection and trapping of tunnel-ionized electrons into laser-produced wakes. *Phys. Rev. Lett.* **104**, 025003 (2010).
44. Chen, M., Sheng, Z.-M., Ma, Y.-Y. & Zhang, J. Electron injection and trapping in a laser wakefield by field ionization to high-charge states of gases. *J. Appl. Phys.* **99**, 056109 (2006).
45. Pícol, L. et al. High efficiency of lutetium silicate scintillators, ce-doped lps, and lyso crystals. *IEEE Trans. Nucl. Sci.* **51**, 1084–1087 (2004).
46. Fleck, K., Cavanagh, N. & Sarri, G. Conceptual design of a high-flux multi-gev gamma-ray spectrometer. *Sci. Rep.* **10**, 9894 (2020).
47. Dong, Y. et al. Absolute x-ray calibration of an amersham imaging plate scanner. *Rev. Sci. Instrum.* **91**, 033105 (2020).
48. Won, J. et al. Monte carlo study of imaging plate response to laser-driven aluminum ion beams. *Appl. Sci.* **11**, 820 (2021).

### Acknowledgements

This work was supported by the National Research Foundation of Korea (NRF) grant funded by the Korea government (MSIT) (No. 2023R1A2C1002912) and by the Institute for Basic Science under IBS-R012-D1.

### Author contributions

C.R., C.H.N. and W.B. conceived the experiment. J.S., Y.N., M.M., C.I.H., H.K., S.L. and J.W. designed and built the setup. J.S., Y.N., M.M., C.I.H., H.K., S.L., J.W. and C.S. performed the experiment and collected data. Y.N., J.S., M.M., H.S. and W.B. analyzed and interpreted the data. Y.N., H.K., and H.S. performed Geant4 simulation. J.S. and Y.N. wrote the manuscript. All authors reviewed the manuscript.

### Competing interests

The authors declare no competing interest.

### Additional information

**Supplementary information** The online version contains supplementary material available at <https://doi.org/10.1038/s42005-024-01527-7>.

**Correspondence** and requests for materials should be addressed to Woosuk Bang.

**Peer review information** *Communications Physics* thanks the anonymous reviewers for their contribution to the peer review of this work. A peer review file is available.

**Reprints and permission information** is available at <http://www.nature.com/reprints>

**Publisher's note** Springer Nature remains neutral with regard to jurisdictional claims in published maps and institutional affiliations.



**Open Access** This article is licensed under a Creative Commons Attribution 4.0 International License, which permits use, sharing, adaptation, distribution and reproduction in any medium or format, as long as you give appropriate credit to the original author(s) and the source, provide a link to the Creative Commons licence, and indicate if changes were made. The images or other third party material in this article are included in the article's Creative Commons licence, unless indicated otherwise in a credit line to the material. If material is not included in the article's Creative Commons licence and your intended use is not permitted by statutory regulation or exceeds the permitted use, you will need to obtain permission directly from the copyright holder. To view a copy of this licence, visit <http://creativecommons.org/licenses/by/4.0/>.

© The Author(s) 2024